Combustion synthesis and electrochemical performance of Li[Li$_{0.2}$Mn$_{0.54}$Ni$_{0.13}$Co$_{0.13}$]O$_2$ with improved rate capability

S.J. Shi, J.P. Tu*, Y.Y. Tang, Y.X. Yu, Y.Q. Zhang, X.L. Wang, C.D. Gu

State Key Laboratory of Silicon Materials, Key Laboratory of Advanced Materials and Applications for Batteries of Zhejiang Province, Department of Materials Science and Engineering, Zhejiang University, Hangzhou 310027, Zhejiang, China

HIGHLIGHTS

► Cathode material Li[Li$_{0.2}$Mn$_{0.54}$Ni$_{0.13}$Co$_{0.13}$]O$_2$ is synthesized by combustion method.
► Alcohol is adopted as both solvent and fuel.
► Initial discharge capacity of 290.1 mAh g^{-1} is obtained at 20 mA g^{-1}.
► High discharge capacity of 165.0 mAh g^{-1} is obtained at 2000 mA g^{-1}.
► Diffusion coefficients of Li$^+$ of 1.07×10^{-14}–1.01×10^{-16} cm^2 s^{-1} is obtained by GITT.

ARTICLE INFO

ABSTRACT

Li-rich layered oxide Li[Li$_{0.2}$Mn$_{0.54}$Ni$_{0.13}$Co$_{0.13}$]O$_2$ is synthesized by combustion reaction using alcohol as both solvent and fuel. X-ray diffraction (XRD), scanning electron microscopy (SEM) and transmission electron microscopy (TEM) show that the oxide synthesized at 800 °C exhibits perfect crystallinity and lattice ordering, and has particle sizes of 50–150 nm. The layered oxide delivers an initial discharge capacity of 290.1 mAh g^{-1} at a current density of 20 mA g^{-1} after activation, and exhibits improved rate capability with high discharge capacities of 238.6 and 165.0 mAh g^{-1} at current densities of 200 and 2000 mA g^{-1} in the voltage range of 2.0–4.8 V, respectively. Low Li-ion diffusion coefficient of 1.07×10^{-14}–1.01×10^{-16} cm^2 s^{-1} is calculated by galvanostatic intermittent titration technique (GITT) during the initial discharge process, indicating that the improved rate capability is mainly attributed to the small particle sizes of the Li-rich oxide.

© 2012 Elsevier B.V. All rights reserved.

1. Introduction

In order to meet the requirement of application in electric vehicles (EVs) and hybrid electric vehicles (HEVs), searching for high capacity, cheap and safe cathode materials has been one of the most important subjects in Li-ion batteries. Li-rich layered oxide with Li$_2$MnO$_3$-like region has been deemed to be a promising candidate due to its high discharge capacity of about 260 mAh g^{-1} when charged to 4.8 V, low cost and security [1–10]. However, such high discharge capacity can only be obtained at extremely low current densities. It is reported by Liu et al. that the bare Li[Li$_{0.2}$Mn$_{0.54}$Ni$_{0.13}$Co$_{0.13}$]O$_2$ could only deliver a discharge capacity of 93 mAh g^{-1} at 1250 mA g^{-1}, about 40% retention of that at 12.5 mA g^{-1} [6]. The unsatisfactory rate capability is ascribed to the Li$_2$MnO$_3$-like region with poor conductivity and the transformation from xLi$_2$MnO$_3$·(1 − x)LiMO$_2$ to Li$_x$MO$_2$ (M = Mn, Co, Ni) [11,12].

In addition, electrochemical performances of cathode materials effectively depend on their morphology and particle size [13,14]. The cathode materials with nanoscaled particles showed an improvement in rate capability due to large specific surface area [15,16]. Simultaneously, the synthesis route employed will deeply affect the morphology and particle size. Currently, many methods have been used to synthesize xLi$_2$MnO$_3$·(1 − x)LiMO$_2$, such as co-precipitation process [4,17–19], microwave heating process [20], sol–gel process [12,21,22], ion-exchange reaction [23] and solid reaction process [24]. Furthermore, combustion method has already been successfully used to synthesize cathode materials with fuel such as sucrose [25–29], urea [30,31], PVA [32], citric acid [33], gelatin [34] and so on [35,36]. For the Li-rich cathode material Li[Li$_{0.2}$Mn$_{0.54}$Ni$_{0.13}$Co$_{0.13}$]O$_2$, it was generally prepared by co-precipitation [7,8,18,37–39] but seldom reported by other methods. In an aim to improve the rate capability of Li[Li$_{0.2}$Mn$_{0.54}$Ni$_{0.13}$Co$_{0.13}$]O$_2$, the combustion method was adopted to synthesize the Li-rich oxide with fuel of sucrose, and its rate capability was improved [15,26].

* Corresponding author. Tel.: +86 571 87952856; fax: +86 571 87952573.
E-mail addresses: tujp@zju.edu.cn, tujplab@zju.edu.cn (J.P. Tu).

In this present work, the combustion reaction is also used to synthesize $Li[Li_{0.2}Mn_{0.54}Ni_{0.13}Co_{0.13}]O_2$ with alcohol as both solvent and fuel without a sol−gel process in water. After calcination, the Li-rich oxide with well-formed layered structure exhibits the improved rate capability.

2. Experimental

In a typical synthesis, stoichiometric amounts of $LiNO_3$ (8.52 g), $Ni(NO_3)_2 \cdot 6H_2O$ (3.78 g), $Co(CH_3COO)_2 \cdot 4H_2O$ (3.24 g) and $Mn(CH_3COO)_2 \cdot 4H_2O$ (13.23 g) were dissolved in 40 ml alcohol. Among them, 3 wt.% excess Li source was added to compensate the lost during calcination treatment. Fierce stir was performed until a transparent solution was obtained. Then the resulting solution was poured into a 300 ml corundum crucible. The crucible was put into a chamber furnace which was pre-heated to 500 °C in air. The combustion reaction finished less than 5 min. Then, the combustion product was ground in a carnelian mortar and again calcined at 700 °C, 800 °C and 900 °C in air for 16 h to get the layered oxide Li$[Li_{0.2}Mn_{0.54}Ni_{0.13}Co_{0.13}]O_2$. The as-synthesized oxides were named as LMNCO-700, LMNCO-800 and LMNCO-900 for short.

The morphologies and structures of the as-synthesized powders were characterized using field emission scanning electron microscopy (FESEM, S-4800) and transmission electron microscopy (TEM, Tecnai G2 F30 S-Twin). XRD measurements were collected on a Rigaku D/Max-2550pc X-ray diffractometer, using CuKα radiation at 40 kV and 250 mA from 2θ degree of 10.0–80.0°, with an increasing step of 0.02° and counting duration of 1.0 s for each step. The unit-cell lattice parameters were obtained by Rietveld refinement of the powder XRD data using the software Maud. The specific surface areas of the powders were measured following the multipoint Brunauer−Emmett−Teller (BET) procedure from the N_2 adsorption−desorption isotherms using an AUTOSORB-1-C gas sorption analyzer.

The working electrodes were prepared by a slurry coating procedure. The slurry consisted of 85 wt.% oxide powders, 10 wt.% carbon conductive agent and 5 wt. % polyvinylidene fluoride (PVDF) was coated on aluminum foil. The mass density of the active material loaded on aluminum foil is 2.26−2.83 mg cm^{-2}. After drying at 90 °C for 24 h in vacuum, the samples were pressed under a pressure of 20 MPa. A metallic lithium foil served as the anode, 1 M $LiPF_6$ in ethylene carbonate (EC)−dimethyl carbonate (DMC) (1:1 in volume) was used as the electrolyte, and a polypropylene micro-porous film (Cellgard 2300) as the separator. The coin-type cells were assembled in an argon-filled glove box with H_2O concentration below 1 ppm. The galvanostatic discharge−charge tests were performed on a LAND battery program-control test system (Wuhan, China) between 2.0 and 4.8 V at the charge−discharge current densities from 20 to 2000 mA g^{-1} at room temperature. Galvanostatic intermittent titration technique (GITT) was also conducted on this apparatus at room temperature in the voltage range of 2.0−4.8 V. Cyclic voltammetry (CV) test was carried out on an electrochemical workstation (CHI660C) in the potential window of 2.0−5.0 V (vs. Li/Li$^+$) at a scan rate of 0.1 mV s^{-1}. Electrochemical impedance spectroscopy (EIS) measurements were performed on this apparatus using a three-electrode cell with the layered oxides as the working electrode, metallic lithium foil as both the counter and reference electrodes. The amplitude of the AC signal was 5 mV over a frequency range from 100 kHz to 10 mHz at different charge states.

3. Results and discussion

3.1. Material characterization

Fig. 1(a)−(d) shows the XRD patterns of the oxides synthesized at different temperatures. For all the XRD patterns, except the super lattice peaks between 20° and 25°, the other peaks can be indexed the α-NaFeO$_2$ structure with space group R-3m. However, the peaks of the powder after combustion reaction at 500 °C without further calcination are weak and broad, and no distinct splitting (006)/(102) and (108)/(110) peak is observed. It indicates that the combustion product has poor crystallinity and needs to be further calcined for high crystallinity. The weak peaks between 20° and 25° for the calcined products, as clearly shown in Fig. 1(e), are consistent with the LiMn$_6$ cation arrangement that occurs in the transition metal layers of Li$_2$MnO$_3$ region or nano-domains, which can be indexed to the monoclinic unit-cell C2/m [40,41]. No peak for any impurity phase is detected in these patterns, indicating high purity of the oxides. In addition, as the calcination temperature increases, the weak peaks with respect to the LiMn$_6$ cation arrangement become more symmetrical and sharper (Fig. 1(e)). The single broad peak at 20.9° of the layered oxides synthesized at a relatively low temperature is attributed to an increase in the amount of the stacking faults (shifting of the TM layers) perpendicular to the layered (001) direction [42]. The role of the stacking faults on the electrochemical performances of the cathode material is unclear. However, from thermodynamics, the introduction of stacking faults and other defects may increase the energy state of the material, which may decrease the activation barrier for Li$^+$ diffusion and allow Li$^+$ to be extracted at a relatively low potential. Apparently, it will make the activation of the Li$_2$MnO$_3$ region during charging easier to some degree. Further studies of these are in progress.

From the Rietveld refinements, the lattice parameters of the layered oxides synthesized at 700 °C, 800 °C and 900 °C are calculated as $a = 2.8545(4)$ Å, $c = 14.2366(1)$ Å; $a = 2.8542(9)$ Å, $c = 14.2534(3)$ Å; $a = 2.8533(2)$, $c = 14.2440(9)$ Å, respectively, as shown in Table 1. It has been reported that the ordering of the oxide structure can be indicated from the XRD patterns with the I_{003}/I_{104} and $(I_{006} + I_{012})/I_{101}$ (R factor) intensity ratios, the lattice parameter ratios of c/a, and the degree of the (006)/(102) and (108)/(110) peak splitting [14,43]. The ratios of c/a and the value of I_{003}/I_{104}, $(I_{006} + I_{012})/I_{101}$ are also shown in Table 1. All the calcined powders have high c/a values, and the c/a value of LMNCO-800 reaches the maximum. Likewise, the R factors of all the oxides are small. The smaller the R factor is, the better the hexagonal ordering is. In addition, LMNCO-800 and LMNCO-900 have much larger value of I_{003}/I_{104} than that of LMNCO-700, indicating better ion arrangement for LMNCO-800 and LMNCO-900. Furthermore, much more distinct splitting (006)/(102) and (108)/(110) peaks appear in LMNCO-800 and LMNCO-900.

A SEM image of the powder after combustion reaction is shown in Fig. 2(a). Because of the fast reaction within 5 min and low temperature of 500 °C, the particles exhibit poor crystallinity, and no ordered layered structure is obtained which has been proved in the XRD section. Thus, further calcination is necessary to get the layered structure with perfect crystallinity. Furthermore, in such a short reaction time, precipitation and agglomeration would not happen. And Mn, Co, Ni ions distributed much more homogeneously in solution than other states, such as co-precipitation or mechanical mixture. SEM images of the oxide powders after calcination at different temperatures are shown in Fig. 2(b)−(d). The as-synthesized powders have homogeneous particles. The specific surface area of LMNCO-800 is about 7.82 m^2 g^{-1} obtained by BET test. However, as the calcination temperature increases to 900 °C, the particle sizes of 200−300 nm and BET area of 4.84 m^2 g^{-1} are obtained due to the grain growth at high temperature (Fig. 2(d)).

Fig. 3 shows the TEM images of Li[Li$_{0.2}$Mn$_{0.54}$Ni$_{0.13}$Co$_{0.13}$]O$_2$ synthesized at 800 °C. The oxide particles are 50−150 nm in sizes (Fig. 3(a)). The HRTEM image shows that the particle has perfect crystallinity with distinct lattice fringes (Fig. 3(b)). The distance
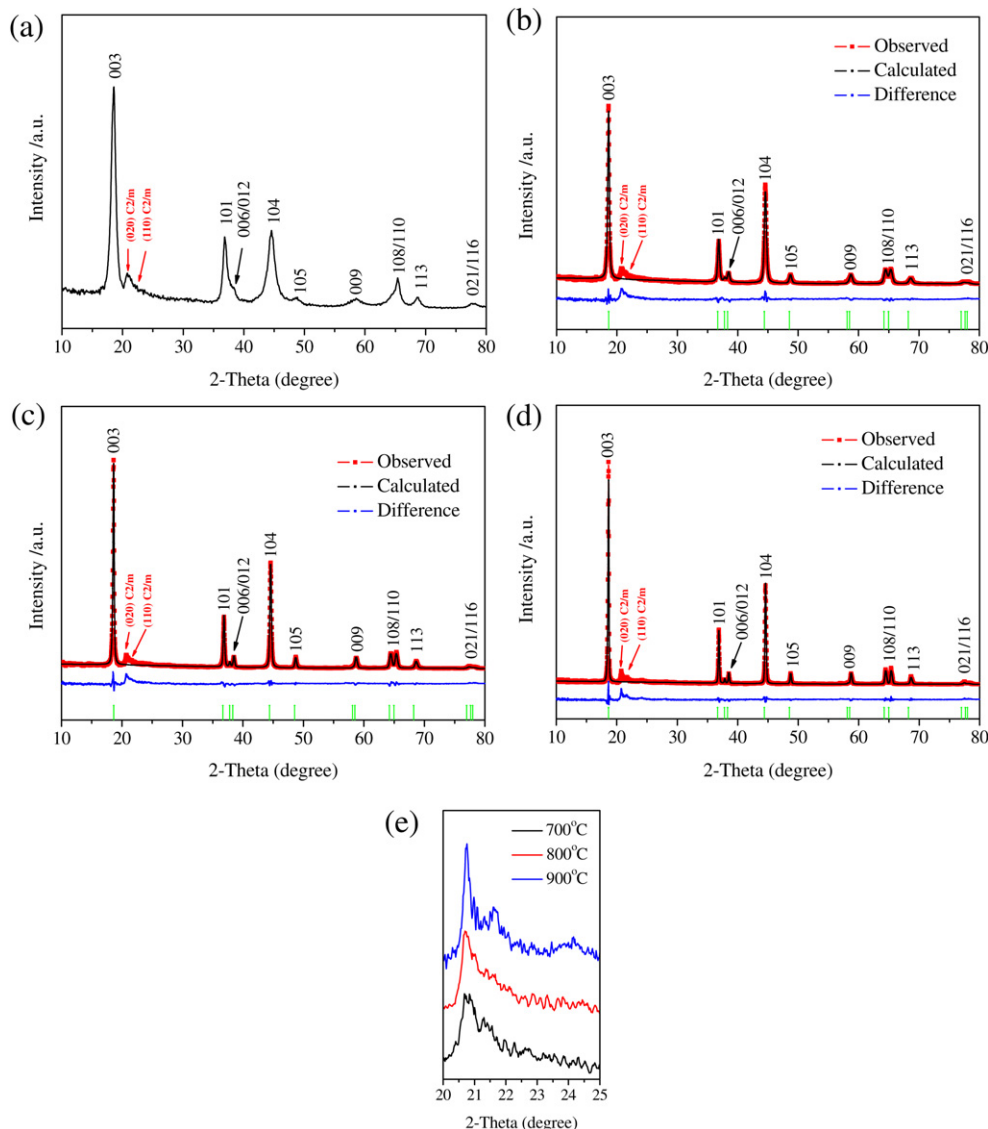
Fig. 1. XRD patterns of Li[Li$_{0.2}$Mn$_{0.54}$Ni$_{0.13}$Co$_{0.13}$]O$_2$ synthesized at (a) 500 °C, (b) 700 °C, (c) 800 °C and (d) 900 °C. And (e) is the magnification of the XRD patterns (b, c, d) from 20° to 25°.

between the neighboring lattice fringes has an approximate d-spacing value of 4.8 Å, which corresponds to the (003) plane of the hexagonal layered phase.

3.2. Electrochemical properties

Fig. 4(a)–(c) shows the charge–discharge curves of Li[Li$_{0.2}$Mn$_{0.54}$Ni$_{0.13}$Co$_{0.13}$]O$_2$ synthesized at different temperatures at a current density of 20 mA g^{-1} in the voltage range of 2.0–4.8 V. As normal Li-rich layered oxides, there are two charge platforms for

Table 1
Lattice parameters and the ratios of I_{003}/I_{104}, $(I_{006} + I_{012})/I_{101}$ (R factor) calculated from the XRD data.

Sample	$a/\text{Å}$	$c/\text{Å}$	c/a	I_{003}/I_{104}	$(I_{006} + I_{012})/I_{101}$ (R factor)
700 °C	2.8545(4)	14.2366(1)	4.987	1.65	0.321
800 °C	2.8542(9)	14.2534(3)	4.994	1.97	0.279
900 °C	2.8533(2)	14.2440(9)	4.992	2.03	0.256

the initial cycle, one at 3.9 V and the other at about 4.5 V. The one at 4.5 V represents the activation of the Li$_2$MnO$_3$-like region which appears only in the initial cycle. As shown in Fig. 4(a)–(c), from the second cycle, the charge platform at 4.5 V disappears due to the irreversible activation at the initial cycle. Among these oxides, LMNCO-800 has the largest initial charge and discharge capacities of 364.2 and 290.1 mAh g^{-1}, respectively. The charge capacity approaches to the theoretical value (377.1 mAh g^{-1}, calculated from the parent Li[Li$_{0.2}$Mn$_{0.54}$Ni$_{0.13}$Co$_{0.13}$]O$_2$). However, the initial coulombic efficiency is low, only about 79.7%, large capacity is lost during the initial cycle. The lost capacity is ascribed to the irreversible removal of Li$_2$O from the Li$_2$MnO$_3$ region, the degradation of electrolyte and SEI forming. Among them, the removal of Li$_2$O from the Li$_2$MnO$_3$ region is the main reason for the low initial coulombic efficiency due to its irreversibility [44,45]. The electrochemical inactive Li$_2$MnO$_3$ region became active after removing of Li$_2$O from the lattice during the activation process at about 4.5 V. However, the initial discharge capacity surpasses the theoretic value (276 mAh g^{-1}, calculated from LiMO$_2$, M = Mn, Co, Ni, after activation). It is reported that anomalously high capacity above the

Fig. 2. SEM images of Li[Li$_{0.2}$Mn$_{0.54}$Ni$_{0.13}$Co$_{0.13}$]O$_2$ powders synthesized at (a) 500 °C, (b) 700 °C, (c) 800 °C and (d) 900 °C.
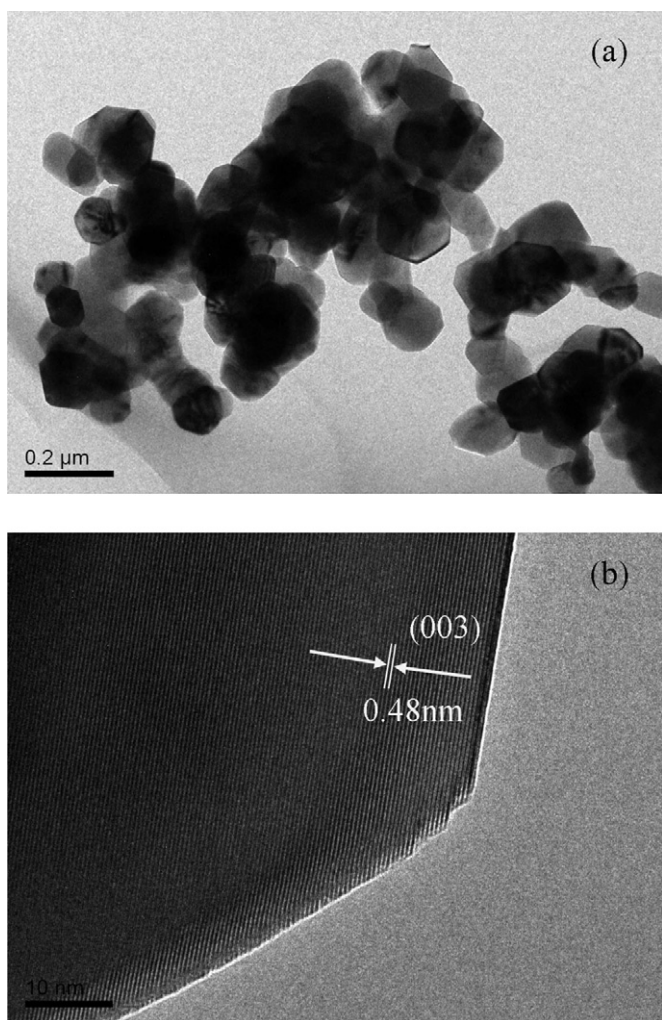
Fig. 3. TEM images of Li[Li$_{0.2}$Mn$_{0.54}$Ni$_{0.13}$Co$_{0.13}$]O$_2$ powder synthesized at 800 °C.

theoretically expected value can be obtained from Li[Li$_{0.2}$Mn$_{0.54}$Ni$_{0.13}$Co$_{0.13}$]O$_2$ [45,46]. Although the origin of the exceptionally high capacity is not yet known, it has been speculated that the anomalous capacity is due to oxygen ion vacancies, which are attributed to the removing of Li$_2$O during the first cycle activation. The as-produced oxygen ion vacancies which were partly maintained temporarily could accommodate the Li$^+$ during the following discharge process, leading to the anomalous capacity for the initial cycle [45,46]. LMNCO-900 also has high charge and discharge capacities of 352.7 and 286.2 mAh g^{-1} at a current density of 20 mA g^{-1}, respectively. However, LMNCO-700 which owns poor layered structure exhibits the lowest initial charge and discharge capacities of 311.3 and 258.4 mAh g^{-1}, respectively. Fig. 4(d) shows the cycle performance of the oxides at a current density of 20 mA g^{-1}. The discharge capacities decrease slowly and reach stable at about 250 mAh g^{-1} for LMNCO-800 and LMNCO-900, while the discharge capacity of LMNCO-700 decreases rapidly and is about 200 mAh g^{-1} after 50 cycles. It can also been observed from the 50th charge–discharge curves in Fig. 4(a)–(c).

Rate capability of Li[Li$_{0.2}$Mn$_{0.54}$Ni$_{0.13}$Co$_{0.13}$]O$_2$ is displayed in Fig. 5 from current density of 20–2000 mA g^{-1} between 2.0 V and 4.8 V. The cells were charged and discharged at the same current density. LMNCO-800 has the best rate capability, and the discharge capacities of 290.1, 253.0, 238.6, 227.7, 211.9, 186.1 and 165.0 mAh g^{-1} are obtained at current densities 20, 40, 100, 200, 400, 1000 and 2000 mA g^{-1}, respectively. The rate capability obtained here is much higher than that of the pristine materials prepared by other methods [6,7,12]. It is partly attributed to the well-formed layered structure and excellent crystallinity. Furthermore, small particle size obtained by solution combustion reaction also contributes a lot due to short Li$^+$ diffusion path and large surface area. However, LMNCO-700 which also has a similar particle size does not exhibit such high rate capability due to the faulty structure. Likewise, LMNCO-900 with large particle size exhibits the worst rate capability though well-formed layered structure is obtained as that of LMNCO-800. It seems that the
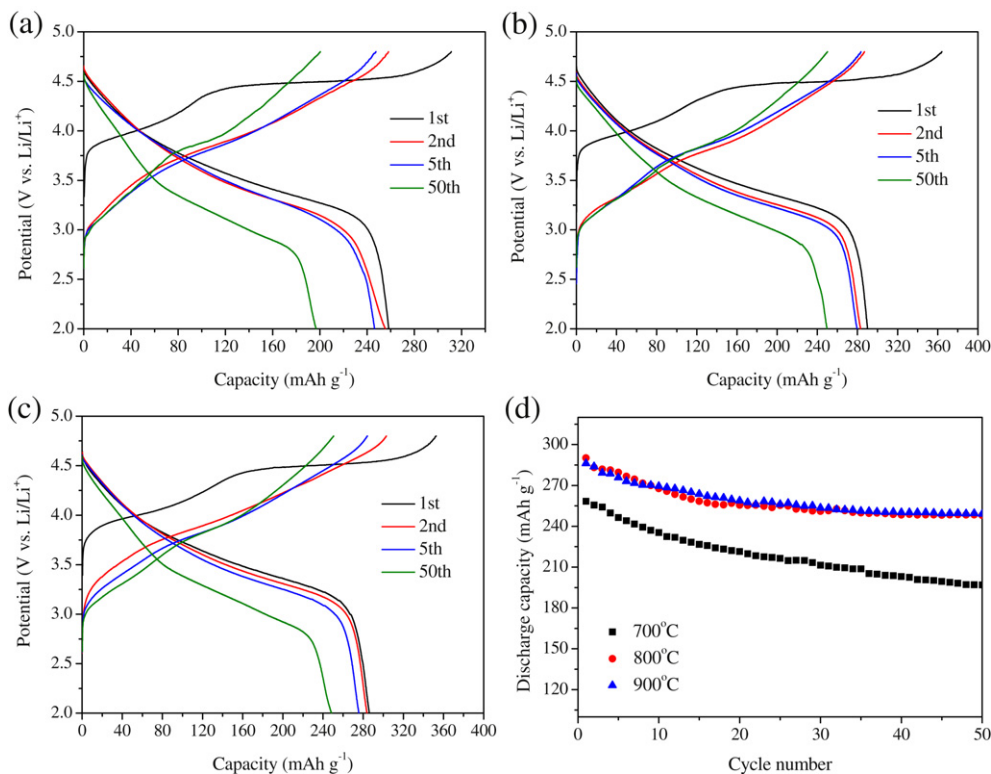
Fig. 4. Charge−discharge curves of Li[Li$_{0.2}$Mn$_{0.54}$Ni$_{0.13}$Co$_{0.13}$]O$_2$ synthesized at (a) 700 °C, (b) 800 °C, (c) 900 °C; (d) cycle performance of Li[Li$_{0.2}$Mn$_{0.54}$Ni$_{0.13}$Co$_{0.13}$]O$_2$ synthesized at different temperatures at a current density of 20 mA g^{-1}.

intrinsic conductivity of Li-rich layered oxide is poor, and the transformation from xLi$_2$MnO$_3$·(1 − x)LiMO$_2$ to Li$_x$MO$_2$ (M = Mn, Co, Ni) will disorder the well-formed crystal lattice, leading to low Li$^+$ diffusion, which is accordant with the result of GITT later. Thus, the effect of particle size is much more important for the rate capability. Only LMNCO-800 with both small particle size and well-formed crystal lattice can exhibit such excellent rate capability.

Fig. 6 shows the initial charge−discharge capacity of all the electrodes at different current densities. The initial charge process can be divided to two parts. The first one is the Li-extraction from the structure of space group R-3m accompanying with the

oxidation of mainly Ni^{2+}/Ni^{4+}. And the second one is the activation of the Li$_2$MnO$_3$-like region. It is clearly shown that as the charge−discharge current density increases, the capacity contribution of the second part (the platform at 4.5 V) decreases faster than that of the first part. The capacity of the activation part is about 210 mAh g^{-1} at a current density of 20 mA g^{-1}, about 67.7% of the total capacity of both platforms at 3.9 V and 4.5 V for LMNCO-700, which is accordant with the theoretical value (66.7%, calculated from 0.6Li[Li$_{1/3}$Mn$_{2/3}$]O$_2$·0.4Li[Mn$_{1/3}$Ni$_{1/3}$Co$_{1/3}$]O$_2$). The similar results are also obtained for both LMNCO-800 and LMNCO-900. However, at 2000 mA g^{-1}, the capacity contribution of the activation part decreases, less than 25% for LMNCO-700. LMNCO-800 has the largest capacity contribution proportion of about 40%. LMNCO-900 has the least and the platform at 4.5 V almost disappears. That is due to the poor electron conductivity of the Li$_2$MnO$_3$-like region. LMNCO-800 has the largest initial discharge capacity at different current densities, 236.6, 184.2 and 147.3 mAh g^{-1} at 200, 1000 and 2000 mA g^{-1}, respectively. Furthermore, since the proportion of the activation charge capacity in total capacity is much smaller than the theoretical value at high current density, it indicates that the activation of the Li$_2$MnO$_3$-like region is not thoroughly performed at the initial cycle. It could also be proved at the cycle tests later.

Fig. 7 shows the cycle performance of Li[Li$_{0.2}$Mn$_{0.54}$Ni$_{0.13}$Co$_{0.13}$]O$_2$ at current densities from 200 to 2000 mA g^{-1} in the voltage of 2.0−4.8 V. It is clear that the cycle stability is improved for the oxides with the increased calcination temperature except for that at a high current density of 2000 mA g^{-1}. LMNCO-900 may not endure such high current density, so that the discharge capacity decreases so fast. LMNCO-700 has the worst cycle stability due to the poor crystallinity. In a word, LMNCO-800 has the best colligation electrochemical performance with high discharge capacity and medium capacity retention at various current densities. The discharge capacity retention of LMNCO-800 is 79.9%, 82.6% and
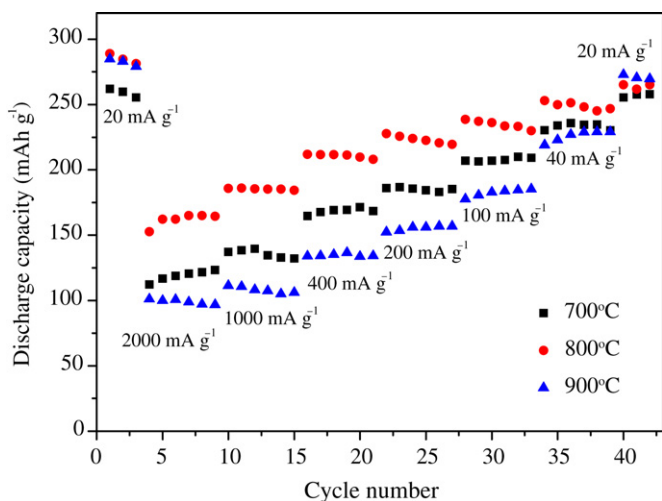

Fig. 5. Rate capability of Li[Li$_{0.2}$Mn$_{0.54}$Ni$_{0.13}$Co$_{0.13}$]O$_2$ synthesized at different temperatures, the cells were charged and discharged at the same current densities.
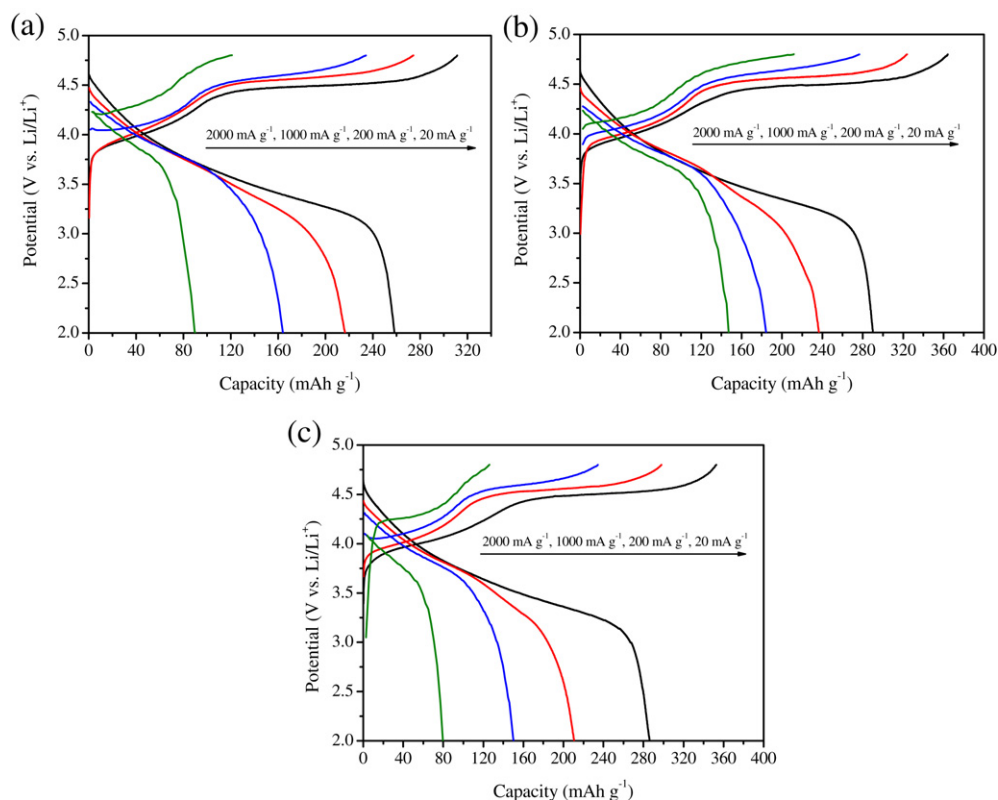
Fig. 6. Initial charge–discharge curves of Li[Li$_{0.2}$Mn$_{0.54}$Ni$_{0.13}$Co$_{0.13}$]O$_2$ synthesized at (a) 700 °C, (b) 800 °C and (c) 900 °C at different current densities.

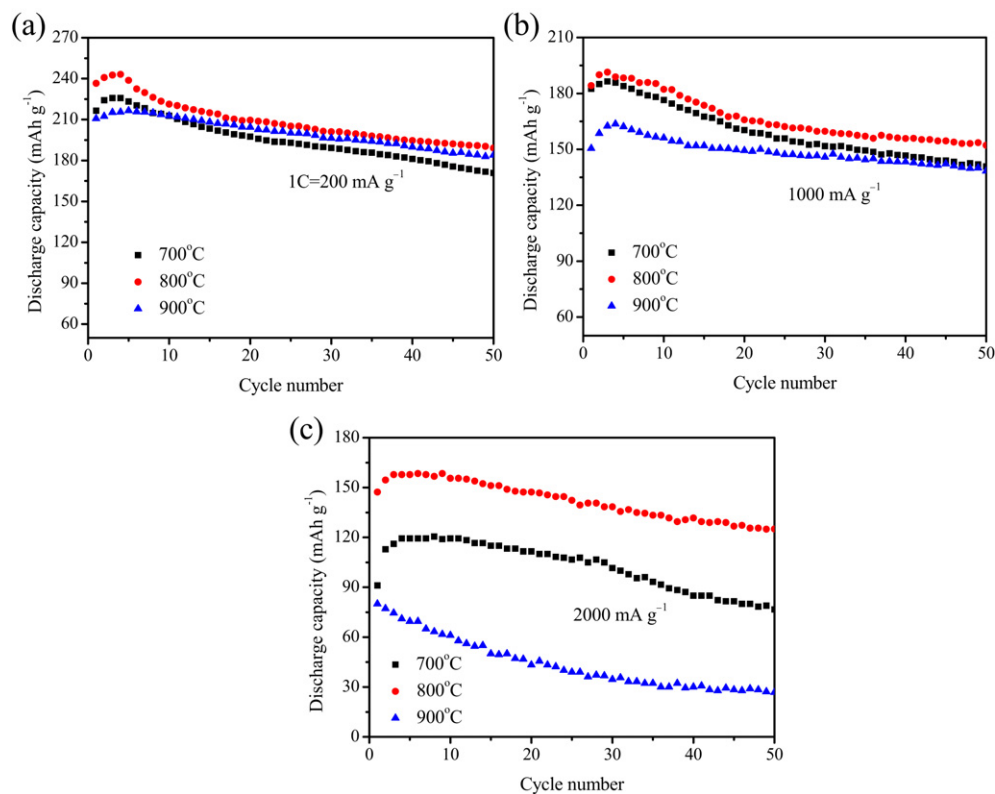**Fig. 7.** Cycle performance of Li[Li$_{0.2}$Mn$_{0.54}$Ni$_{0.13}$Co$_{0.13}$]O$_2$ synthesized at different temperatures at different current densities.

84.9% at current densities of 200, 1000 and 2000 mA g^{-1}, respectively, with respect to the initial discharge capacity after 50 cycles. Two main factors have been demonstrated to affect the cycle stability [2,47–49]. One is the dissolution of the metal ions, especially the manganese ion during charge–discharge process. The mechanism of the Mn dissolution can be explained as follows:

$$Mn^{3+} \xrightarrow{charge-discharge} Mn^{4+} + Mn^{2+} \qquad (1)$$
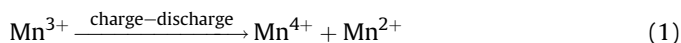
The lower the calcination temperature is, the lower the oxidation state of Mn is. Not all the Mn ions are in the oxidation state of 4+, part will stay at the oxidation state of 3+, and this part of Mn will easily be dissolved. In addition, during discharging to a low potential, part of Mn^{4+} will be reduced to Mn^{3+}. The dissolution will seriously destroy the oxide surface and unsatisfactory SEI film will form. The other is the Jahn–Teller distortion during the cycling process. If Li[Li$_{0.2}$Mn$_{0.54}$Ni$_{0.13}$Co$_{0.13}$]O$_2$ completely delithiated during charge, then it would yield Mn$_{0.675}$Ni$_{0.1625}$Co$_{0.1625}$O$_2$ in which the manganese ions were tetravalent, higher than that expected for a potentially damaging Jahn–Teller distortion [45].

In addition, it distinctly reveals that at the beginning of the cycling, there is an activation process, in which the discharge capacity increases to a top value and then decreases steadily. Such phenomenon is not observed for the cycling at low current density. The reason has been mentioned above. At an elevated current density, the activation of the Li$_2$MnO$_3$-like region at about 4.5 V in the initial cycle is not performed thoroughly. Thus, the activation is going on for the initial several cycles accompanying with the increase of discharge capacity.

CV tests were performed to further understand the oxides synthesized by alcohol-assist combustion method. Fig. 8 shows the CV curves of Li[Li$_{0.2}$Mn$_{0.54}$Ni$_{0.13}$Co$_{0.13}$]O$_2$ for the initial three cycle. The initial CV curve for the oxidation section is sharp, symmetrical and accordant with the initial charge curve. There are two main anodic peaks, one at about 3.9 V and another at about 4.6 V (vs. Li/Li$^+$). The peak at low potential is ascribed to the extraction of Li$^+$ from the LiMO$_2$ (M = Mn, Ni, Co) structure. And another peak at 4.6 V is ascribed to the activation of the Li$_2$MnO$_3$ region, extraction of Li$^+$ from Li[Li$_{1/3}$Mn$_{2/3}$]O$_2$. It has been demonstrated that when the Li$_2$MnO$_3$-based material is charged above 4.4 V, the excess Li will extract from the Li$_2$MnO$_3$ region, accompanying with loss of O

[45]. Interestingly, the inactive Li[Li$_{1/3}$Mn$_{2/3}$]O$_2$ becomes active [MnO$_2$], and during the following discharge process, a high initial discharge capacity of 290 mAh g^{-1} is obtained for LMNCO-800, exceeding the theory capacity (~276 mAh g^{-1}, calculated from the mass of the active LiMn$_{0.675}$Ni$_{0.1625}$Co$_{0.1625}$O$_2$) after electrochemical activation when charged and discharged between 2.0 and 5.0 V. However, at the second cycle, the activation peak disappears and a broad peak appears at 3.85 V which is the main anodic peak for the newly formed LiMn$_{0.675}$Ni$_{0.1625}$Co$_{0.1625}$O$_2$ (supposing that after initial activation all the Li is removed from Li[Li$_{0.2}$Mn$_{0.54}$Ni$_{0.13}$Co$_{0.13}$]O$_2$. Thus, [Mn$_{0.54}$Ni$_{0.13}$Co$_{0.13}$]O$_{1.6}$ is obtained and if Li is re-inserted, we can obtained LiMn$_{0.675}$Ni$_{0.1625}$Co$_{0.1625}$O$_2$). Two cathodic peaks are evident during the discharge process. Although it is impossible to differentiate the reduction processes of the individual Mn, Ni and Co from the data, it is believed from the theoretical studies that the process at about 4.5 V may be associated with the occupation of tetrahedral sites by lithium within the extensively delithiated layer and the lower voltage processed at ~3.25 V to the occupation of octahedral sites, in agreement with
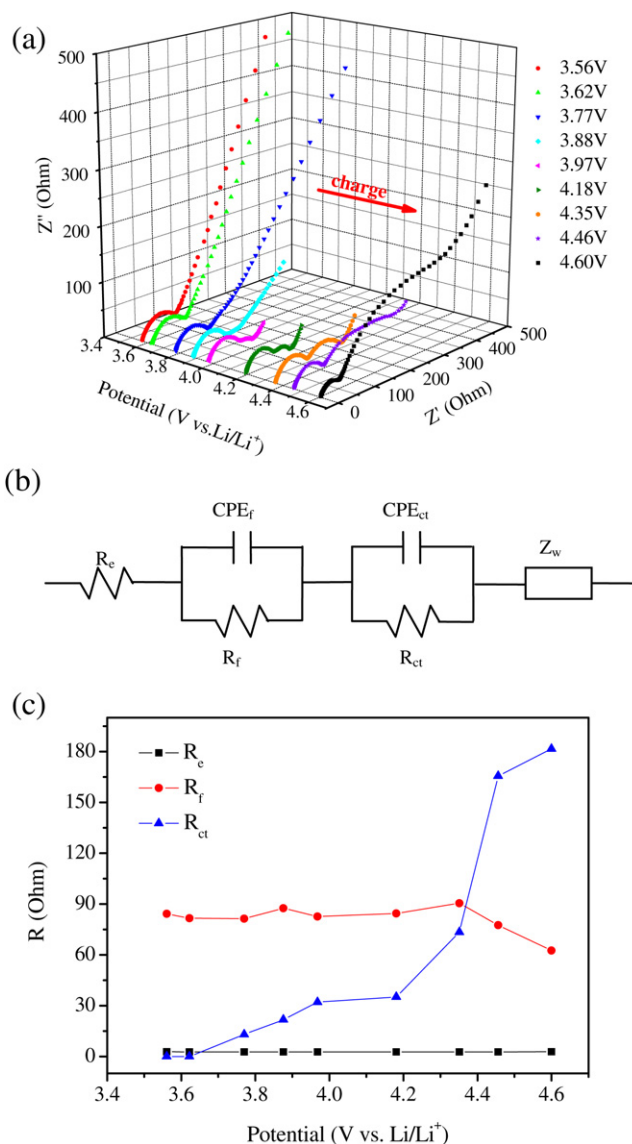

Fig. 9. (a) Nyquist plots of Li[Li$_{0.2}$Mn$_{0.54}$Ni$_{0.13}$Co$_{0.13}$]O$_2$ synthesized at 800 °C in the initial cycle at different charge states, (b) equivalent circuit performed to fit the curves in (a), (c) variation of R_e, R_f and R_{ct} with the potential.
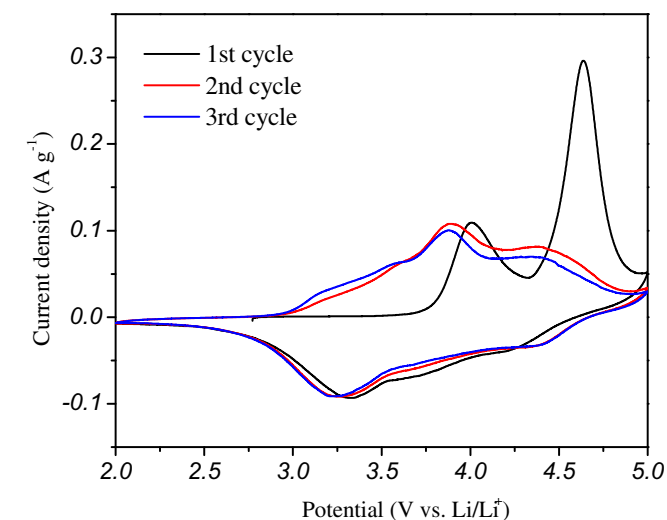

Fig. 8. CV curves of Li[Li$_{0.2}$Mn$_{0.54}$Ni$_{0.13}$Co$_{0.13}$]O$_2$ synthesized at 800 °C for the initial three cycles (scan rate: 0.1 mV s^{-1}, potential range: 2.5–4.8 V).

the reports of Hayley et al. [50]. The two processes still appear at the third cycle which proves both of the reaction processes are reversible.

In order to further understand the Li[Li$_{0.2}$Mn$_{0.54}$Ni$_{0.13}$Co$_{0.13}$]O$_2$ synthesized at 800 °C, a detailed study of Nyquist plots at different open circuit voltages was carried out during the initial charge process at a current density of 20 mA^{-1}. Fig. 9(a) shows the Nyquist plots of LMNCO-800 at different charge states in the initial cycle. The shapes of the Nyquist plots at different states are a little different. The points of 3.56, 3.62 and 3.77 V are chosen as the beginning of the charge, 3.88, 3.97, 4.18 and 4.35 V as the charge platform for delithiated from the structure of LiMO$_2$ (M = Mn, Ni, Co), and 4.46 V, 4.60 V as the delithiated from the Li$_2$MnO$_3$-like region. After 3.97 V, the curves are composed of a small interrupt and a semicircle in the high frequency, a semicircle in the high to medium frequency and a quasi-straight line in the low frequency. The small interrupt in the high frequency is almost the same for the

oxide electrode at about 2.7 Ω, which corresponds to the solution resistance R_e. The small semicircle in the high frequency is assigned to the impedance (R_f) of Li$^+$ diffusion in the surface layer (SEI film); another semicircle in the high to medium frequency is assigned to the impedance of charge-transfer reaction (R_{ct}); and a quasi-straight line in the low frequency is assigned to the diffusion of Li$^+$ in bulk material [5,6]. Before 3.97 V, however, the semicircle in the high to medium frequency disappears due to the dinky R_{ct}, only the semicircle in high frequency and the quasi-straight line in the low frequency are observed. In order to further understand Nyquist plots, an equivalent circuit is shown in Fig. 9(b). CEP$_f$, CEP$_{ct}$ and Z_w represent the non-ideal capacitance of the surface layer, non-ideal capacitance of the double-layer and Warburg impedance which refers to the impedance of Li$^+$ diffusion in bulk material, respectively [5,6]. The value of R_e, R_f and R_{ct} for LMNCO-800 at different charge states are calculated and shown in Fig. 9(c). At the beginning of the charge, the charge-transfer impedance is so small that the
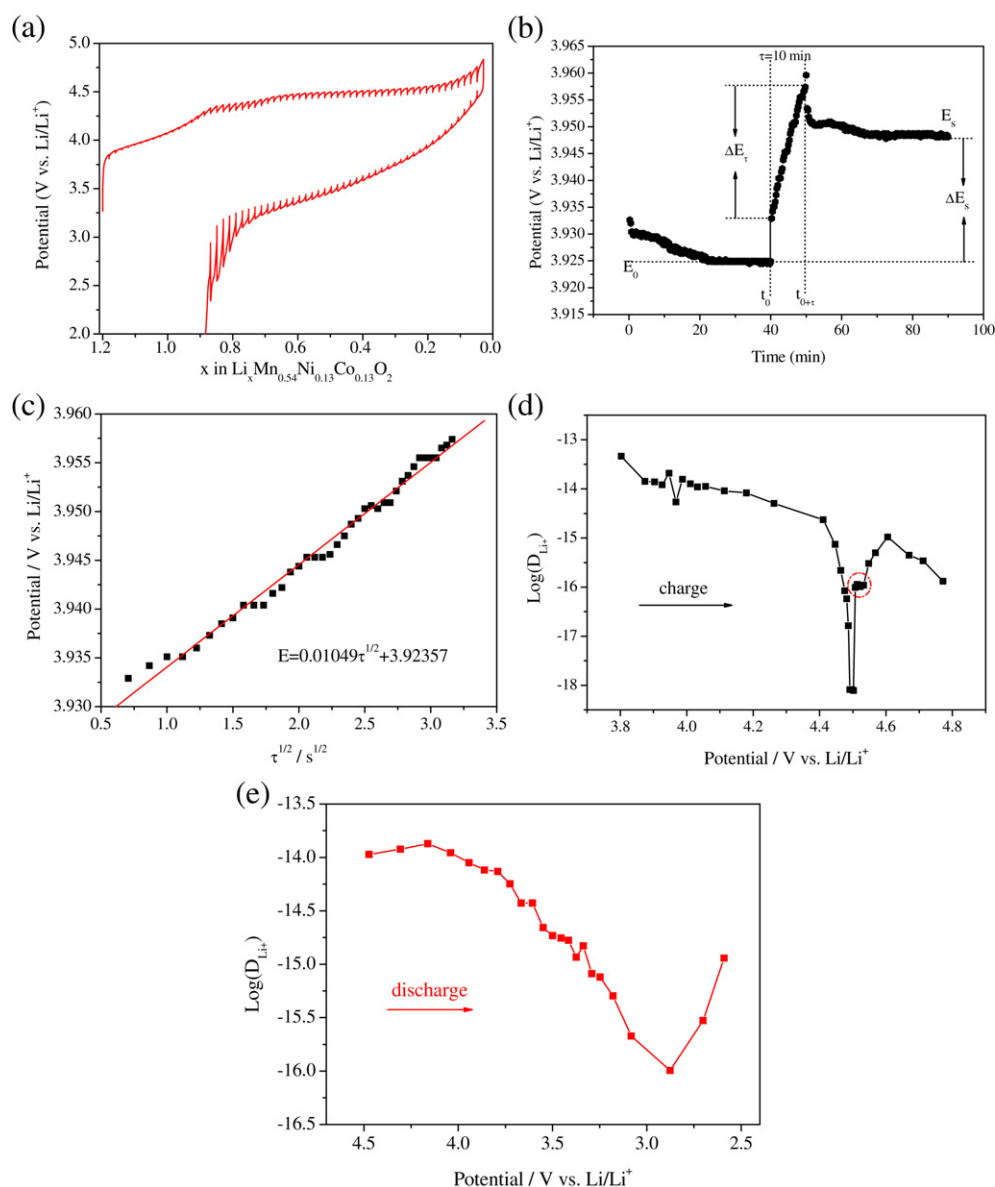

Fig. 10. (a) GITT curves of Li[Li$_{0.2}$Mn$_{0.54}$Ni$_{0.13}$Co$_{0.13}$]O$_2$ for the initial cycle between 2.0 V and 4.8 V (current flux: 40 mA g^{-1}, time interval: 40 min), (b) t vs. E profile of Li[Li$_{0.2}$Mn$_{0.54}$Ni$_{0.13}$Co$_{0.13}$]O$_2$ for a single GITT titration, (c) linear behavior of E vs. $\tau^{1/2}$, (d) diffusion coefficients of Li$^+$ in Li[Li$_{0.2}$Mn$_{0.54}$Ni$_{0.13}$Co$_{0.13}$]O$_2$ at different charge states, (e) diffusion coefficients of Li$^+$ in Li[Li$_{0.2}$Mn$_{0.54}$Ni$_{0.13}$Co$_{0.13}$]O$_2$ at different discharge states.

calculation value is approaching to zero, which indicates the effect of R_{ct} is neglectable comparing to that of the Li^+ diffusion. As the charge process goes on, R_{ct} increases from 32.0 Ω at 3.97 V to 165.6 Ω at 4.46 V. It seems that R_{ct} of the delithiated process from the structure of $LiMO_2$ (M = Mn, Ni, Co) is much smaller than that from the Li_2MnO_3-like region, which is ascribed to the poor conductivity of the Li_2MnO_3-like region. Furthermore, the values of R_f at different charge states are stable at 70−90 Ω, indicating that the surface of the particle does not change a lot. It seems that at the initial charge process, SEI layer is not thicker and this layer is stable.

GITT test was carried out to evaluate Li^+ diffusion in the Li-rich layered oxide. Fig. 10(a) shows the GITT curves of $Li[Li_{0.2}Mn_{0.54}Ni_{0.13}Co_{0.13}]O_2$ synthesized at 800 °C during the initial charge−discharge process from 2.0 V to 4.8 V. The chemical diffusion coefficient of Li^+ (D_{Li^+}) is calculated according to Eq. (2) derived by Weppner and Huggins as follows [51]:

$$D_{Li^+} = \frac{4}{\pi}\left(\frac{mV_M}{MA}\right)^2\left(\frac{\Delta E_s}{\tau(dE_\tau/d\sqrt{\tau})}\right)^2\left(\frac{\tau << L^2}{D_{Li^+}}\right) \tag{2}$$

where V_M is the molar volume of the compound, which is 20.21 $cm^3\ mol^{-1}$ deduced from the crystallographic data. M and m are the molecular weight and mass of the $Li_{1.131}Mn_{0.504}Ni_{0.243}Co_{0.122}O_2$, respectively. A is the interface between the active material and electrolyte, which is based on the result of the BET test (7.82 $m^2\ g^{-1}$). L is the radius of the active particle. Fig. 10(b) shows a typical t vs. E profile for a single titration. If E vs. $\tau^{1/2}$ shows a straight line behavior over the entire time period of current flux, as shown in Fig. 10(c), Eq. (2) can be further simplified as follows [51]

$$D_{Li^+} = \frac{4}{\pi\tau}\left(\frac{mV_M}{MA}\right)^2\left(\frac{\Delta E_s}{\Delta E_\tau}\right)^2 \tag{3}$$

Based on Eq. (3) and GITT measurement, the diffusion coefficients of Li^+ at varied voltages can be obtained, as shown in Fig. 10(d) and (e). The results of the charge section have a similar rule to the initial charge curve shown in Fig. 4(a). At the charge process from 3.8 to 4.2 V, the Li^+ probably extracts from the R-3m structure $LiMO_2$ (M = Mn, Ni, Co) region. And a constant D_{Li^+} of about 10^{-14} $cm^2\ s^{-1}$ is obtained at that process. However, D_{Li^+} decreases as the charge process is proceeding and at the end of the first charge platform, a minimum D_{Li^+} of 8.12×10^{-19} $cm^2\ s^{-1}$ is obtained at 4.50 V. As the charge process goes along, the D_{Li^+} increases to about 10^{-16} $cm^2\ s^{-1}$ at the charge platform of 4.52 V (the region in the red (in the web version) cycle in Fig. 10(d)), corresponding to the activation section of the Li_2MnO_3 region. It indicates that the Li^+ diffusion in Li_2MnO_3 region is slower than that in $LiMO_2$ (M = Mn, Ni, Co) region.

Fig. 10(e) shows the variation of D_{Li^+} during the whole discharge process. It decreases almost linearly from 4.2 to 2.9 V, and reaches a minimum value of 1.01×10^{-16} $cm^2\ s^{-1}$ at 2.87 V. The absence of a stable region during the discharge process may be due to the complex dynamics, which is impossible to be differentiated clearly [45]. It can also be proved from the CV curves: a large and broad cathodic peak almost stretches across the whole discharge process, including a lot of lithium-insertion processes [45]. Furthermore, the reactions during the charge−discharge process are extremely complex, which include not only Li^+ diffusion but also oxygen loss, metal ion dissolution and structural rearrangement. Thus, the D_{Li^+} obtained here should be regarded as pseudo or apparent diffusion coefficients [11]. To compare with typical layered oxides such as $LiCoO_2$ (10^{-7}−10^{-11} $cm^2\ s^{-1}$) [52] and $LiNi_{1/3}Co_{1/3}Mn_{1/3}O_2$ (10^{-9}−10^{-10} $cm^2\ s^{-1}$) [53], the D_{Li^+} obtained is extremely small. This is understandable because abundant lattice disorders are produced

during the transformation from $Li_{1.131}Mn_{0.504}Ni_{0.243}Co_{0.122}O_2$ to Li_xMO_2. The resultant crystal lattice is not perfect, which therefore retards the Li^+ diffusion. The excellent rate capability in this work is probably attributed to the small particles obtained by solvent combustion method, which significantly enlarges the interface between the oxide particles and electrolyte and shortens the diffusion distance of Li^+.

4. Conclusions

Alcohol was performed as both solvent and fuel to synthesize layered oxide $Li[Li_{0.2}Mn_{0.54}Ni_{0.13}Co_{0.13}]O_2$ by combustion method without a sol−gel process. The oxide synthesized at 800 °C with particle sizes of 50−150 nm exhibits high discharge capacities of 238.6 and 165.0 mAh g^{-1} at current densities of 200 and 2000 mA g^{-1} in the voltage range of 2.0−4.8 V, respectively. About 57% capacity is retained at 2000 mA g^{-1} with respect to that at 20 mA g^{-1}. The diffusion coefficient of Li^+ calculated by GITT during the initial discharge process is 1.07×10^{-14}−1.01×10^{-16} $cm^2\ s^{-1}$, much smaller than those of typical layered materials, which indicates that the improved rate capability of the oxide is mainly attributed to the small particle sizes.

References

[1] L.J. Long, W. Jie, X.Y. Yao, Electrochim. Acta 56 (2011) 7392.
[2] A. Ito, D. Li, Y. Sato, M. Arao, M. Watanabe, M. Hatano, H. Horie, Y. Ohsaw, J. Power Sources 195 (2010) 567.
[3] J. Li, R. Klöpsch, M.C. Stan, S. Nowak, M. Kunze, M. Winter, S. Passerini, J. Power Sources 196 (2011) 4821.
[4] J. Gao, J. Kim, A. Manthiram, Electrochem. Commun. 11 (2009) 84.
[5] S.J. Shi, J.P. Tu, Y.J. Mai, Y.Q. Zhang, C.D. Gu, X.L. Wang, Electrochim. Acta 63 (2012) 112.
[6] J. Liu, B.R. Jayan, A. Manthiram, J. Phys. Chem. C 114 (2010) 9528.
[7] J.M. Zheng, Z.R. Zhang, X.B. Wu, Z.X. Dong, Z. Zhu, Y. Yang, J. Electrochem. Soc. 155 (2008) A775.
[8] D.Y.W. Yu, K. Yanagida, H. Nakamura, J. Electrochem. Soc. 157 (2010) A1177.
[9] S.K. Martha, J. Nanda, G.M. Veith, N.J. Dudney, J. Power Sources 216 (2012) 179.
[10] S.K. Martha, J. Nanda, G.M. Veith, N.J. Dudney, J. Power Sources 199 (2012) 220.
[11] Z. Li, F. Du, X.F. Bie, J. Phys. Chem. C 114 (2010) 22751.
[12] J.M. Zheng, X.B. Wu, Y. Yang, Electrochim. Acta 56 (2011) 3071.
[13] H.M. Wu, C.V. Rao, B. Rambabu, Mater. Chem. Phys. 116 (2009) 532.
[14] C.X. Cheng, L. Tan, H.W. Liu, X.T. Huang, Mater. Res. Bull. 46 (2011) 2032.
[15] J.M. Amarilla, R.M. Rojas, F. Pico, L. Pascual, K. Petrov, D. Kovacheva, M.G. Lazarraga, I. Lejona, J.M. Rojo, J. Power Sources 174 (2007) 1212.
[16] D. Kovacheva, H. Gadjov, K. Petrov, S. Mandal, M.G. Lazarraga, L. Pascual, J.M. Amarilla, R.M. Rojas, P. Herrero, J.M. Rojo, J. Mater. Chem. 12 (2002) 1184.
[17] F. Wu, H.Q. Lu, Y.F. Su, N. Li, L.Y. Bao, S. Chen, J. Appl. Electrochem. 40 (2010) 783.
[18] J.H. Lim, H. Bang, K.S. Lee, K. Amine, Y.K. Sun, J. Power Sources 189 (2009) 571.
[19] S.H. Kang, M.M. Thackeray, Electrochem. Commun. 11 (2009) 748.
[20] Q.W. Peng, Z.Y. Tang, L.Q. Zhang, X.J. Liu, Mater. Res. Bull. 44 (2009) 2147.
[21] S. Sivaprakash, S.B. Majumder, Solid State Ionics 181 (2010) 730.
[22] Y.J. Wei, K. Nikolowski, S.Y. Zhan, H. Ehrenberg, S. Oswald, G. Chen, C.Z. Wang, H. Chen, Electrochem. Commun. 11 (2009) 2008.
[23] D. Kim, S.-H. Kang, M. Balasubramanian, C.S. Johnson, Electrochem. Commun. 12 (2010) 1618.
[24] S.J. Shi, J.P. Tu, Y.Y. Tang, Y.X. Yu, Y.Q. Zhang, X.L. Wang, J. Power Sources 221 (2013) 300.
[25] O. Haik, S.K. Martha, H. Sclar, Z. Samuk-Fromovich, E. Zinigrad, B. Markovsky, D. Kovacheva, N.y Saliyski, D. Aurbach, Thermochim. Acta 493 (2009) 96.
[26] G. Kim, S. Yi, Y.J. Park, H. Kim, Mater. Res. Bull. 43 (2008) 3543.
[27] B. Markovsky, D. Kovachev, Y. Talyosef, M. Gorova, J. Grinblat, D. Aurbach, Electrochem. Solid State Lett. 9 (2006) A449.
[28] J.M. Amarilla, K. Petrov, F. Picó, G. Avdeev, J.M. Rojo, R.M. Rojas, J. Power Sources 191 (2009) 591.

[29] J.M. Amarilla, R.M. Rojas, J.M. Rojo, J. Power Sources 196 (2011) 5951.
[30] S.N. Kwon, J. Song, D.R. Mumm, Ceram. Int. 37 (2011) 1543.
[31] Z.H. Zhong, N.Q. Ye, H. Wang, Z. Ma, Chem. Eng. J. 175 (2011) 579.
[32] A. Subramania, N. Angayarkanni, T. Vasudevan, Mater. Chem. Phys. 102 (2007) 19.
[33] P. Ghosh, S. Mahanty, R.N. Basu, Mater. Chem. Phys. 110 (2008) 406.
[34] P. Periasamy, N. Kalaiselvi, J. Power Sources 159 (2006) 1360.
[35] P. Manikandan, M.V. Ananth, T.P. Kumar, M. Raju, P. Periasamy, K. Manimaran, J. Power Sources 196 (2011) 10148.
[36] P. Suresh, S. Rodrigues, A.K. Shukla, S.A. Shivashankar, N. Munichandraiah, J. Power Sources 112 (2002) 665.
[37] C.S. Johnson, N. Li, C. Lefief, M.M. Thackeray, Electrochem. Commun. 9 (2007) 787.
[38] Y. Wu, A. Manthiram, Electrochem. Solid State Lett. 9 (2006) A221.
[39] X.J. Guo, Y.X. Li, M. Zheng, J.M. Zheng, J. Li, Z.L. Gong, Y. Yang, J. Power Sources 184 (2008) 414.
[40] J.S. Kim, C.S. Johnson, J.T. Vaughey, M.M. Thackeray, S.A. Hackney, W. Yoon, C.P. Grey, Chem. Mater. 16 (2004) 1996.
[41] W.S. Yoon, S. Iannopollo, C.P. Grey, D. Carlier, J. Gorman, J. Reed, G. Ceder, Electrochem. Solid State Lett. 7 (2004) A167.
[42] D.Y.W. Yu, K. Yanagid, Y. Kato, H. Nakamur, J. Electrochem. Soc. 156 (2009) A417.
[43] S.H. Kang, M.M. Thackeray, C.S. Johnson, J.T. Vaughey, S.A. Hackney, Electrochem. Commun. 8 (2006) 1531.
[44] M.M. Thackeray, S.H. Kang, C.S. Johnson, J.T. Vaughey, R. Benedek, S.A. Hackney, J. Mater. Chem. 17 (2007) 3053.
[45] C.S. Johnson, N. Li, C. Lefief, J.T. Vaughey, M.M. Thackeray, Chem. Mater. 20 (2008) 6095.
[46] W. He, J.F. Qian, Y.L. Cao, X.P. Ai, H.X. Yang, RSC Adv. 2 (2012) 3423.
[47] J. Park, J.H. Seo, G. Plett, W. Lu, A.M. Sastry, Electrochem. Solid State Lett. 14 (2011) A14.
[48] D.H. Jang, Y.J. Shin, S.M. Oh, J. Electrochem. Soc. 143 (1996) 2204.
[49] M. Wohlfahrt-Mehrens, C. Vogler, J. Garche, J. Power Sources 127 (2004) 58.
[50] H.H. Hayley, N. Yabuuchi, Y.S. Meng, S. Kumar, J. Breger, C.P. Grey, Y. Shao-Horn, Chem. Mater. 19 (2007) 2551.
[51] W. Weppner, R.A. Huggins, J. Electrochem. Soc. 124 (1977) 1569.
[52] M. Park, X.C. Zhang, M. Chung, G.B. Less, A.M. Sastry, J. Power Sources 195 (2010) 7904.
[53] K.M. Shaju, G.V.S. Rao, B.V.R. Chowdariz, J. Electrochem. Soc. 151 (2004) A1324.